International Journal of Heat and Mass Transfer 120 (2018) 1020–1030

Contents lists available at ScienceDirect

International Journal of Heat and Mass Transfer

journal homepage: www.elsevier.com/locate/ijhmt

Enhanced boiling heat transfer on nanowire-forested surfaces under subcooling conditions

Donghwi Lee [a,1], Beom Seok Kim [b,1], Hokyu Moon [c], Namkyu Lee [a], Sangwoo Shin [d], Hyung Hee Cho [a,*]

[a] Department of Mechanical Engineering, Yonsei University, 50 Yonsei-ro, Seodaemun-gu, Seoul 120-749, Republic of Korea
[b] DEMO Technology Division, National Fusion Research Institute (NFRI), 169-148 Gwahak-ro Yuseong-gu, Daejeon 34133, Republic of Korea
[c] Tokamak Engineering Department, National Fusion Research Institute (NFRI), 169-148 Gwahak-ro Yuseong-gu, Daejeon 34133, Rpublic of Korea
[d] Department of Mechanical Engineering, University of Hawaii at Manoa, Honolulu, HI 96822, USA

ARTICLE INFO

Article history:
Received 16 June 2017
Received in revised form 21 October 2017
Accepted 21 December 2017
Available online 4 January 2018

Keywords:
Boiling heat transfer
Nanowire-forested surfaces
Subcooling
Thermal stability
Critical heat flux
Nucleation

ABSTRACT

In boiling heat transfer, the emerging issues are the improvement of both the critical heat flux (CHF) and the thermal stability. Nanowire-forested (NF) surfaces and subcooled environments are favorable for improving CHF as well as the thermal stability owing to their distinctive morphology and consequential convection expedition, respectively. In this study, the improvement of CHF and temperature uniformity/stability are evaluated on NF surfaces immersed in de-ionized water with subcooling from 0 to 30 K using a resistance temperature detector (RTD) sensor with five measuring points. NF surfaces catalyze dispersed, confined and fast bubble ebullitions under subcooling conditions, resulting in the delayed bubble coalescences. This lead to the enhancement of CHF accompanying stabilized spatial/temporal temperature variations. We demonstrate that NF surfaces applying 30 K subcooled condition not only significantly improve the thermal stability by reducing spatial/temporal temperature variations to less than 1/5 but also enhance CHF by 4.3 folds, compared to the plain surfaces under the saturated condition. These remarkable enhancements show that NF surfaces can be effective solutions to secure the thermal stability under vigorous boiling conditions.

1. Introduction

Over the past several decades, boiling heat transfer phenomena have attracted a great deal of attention from researchers, prompting widespread application in various industries ranging from large-scale power plants to small-scale electronics. Boiling heat transfer, in which the working fluid undergoes a phase-change from liquid to vapor, has greater heat-transfer capabilities than single-phase convection schemes [1]. Many recent studies have focused on developing practical cooling configurations capable of sustaining harsh thermal loads, namely maximizing the heat-dissipation capacity under stable operating conditions, i.e., increasing the critical heat flux (CHF) and heat transfer uniformity/stability [2–8].

Functional interfacial structures have intrinsic merits in the context of boiling applications; fine structures can attain high surface roughness and increase the heat-transfer area for heat dissipation. Nanoscale or nano-micro-hierarchical structures exhibit strong interfacial hemi-wicking with consequential superhydrophilic wetting, which directly enhances the surface rewetting against surface dry-out. As heterogeneous phase change and sequential two-phase convection are strongly dependent on solid–liquid interfacial characteristics such as roughness and wettability [9–15], researchers have focused on the manipulation of their functionalities for favorable nucleation and hydrodynamic balance against surface dry-out. Recent studies reported CHF can be dramatically improved by employing nanostructures on a boiling surface [10–16]. Because surface wettability and morphology can be controlled by nanoscale surface design, numerous studies have focused on the invention and characterization of novel nanostructures to enhance the heat and mass transfer for practical application [12–20].

The distinctive morphology of nanowire-forested (NF) surfaces, in particular, have shown promising results in their ability to improve CHF and enhance heat transfer stability. As shown in Fig. 1, on the basis of distinctive near-field characteristics of interfacial benefits for boiling concomitant with morphological aspects, we have confirmed that the merits of NF surfaces extend to subcooled boiling. In this regime, NF surfaces readily enhance CHF by suppressing bubble coalescence. As subcooling is a far-field

* Corresponding author.
E-mail address: hhcho@yonsei.ac.kr (H.H. Cho).
[1] These authors contributed equally to this work.

https://doi.org/10.1016/j.ijheatmasstransfer.2017.12.100
0017-9310/

Nomenclature

A	heating area (m^2)
D	diameter (m)
I	current (A)
Ja	Jakob number
k	thermal conductivity (W/mK)
l	latent heat (J/g)
P	pressure (Pa)
q	heat flux (W/cm^2)
r	radius (m)
T	temperature (°C)
t	thickness (m)
V	voltage (V)

Greek letters

γ	surface tension (J/m^2)
Δ	difference
δ	thermal boundary layer thickness (m)
θ	contact angle (°)
ρ	density (kg/m^3)
σ	standard deviation

Subscripts

avg	average
b	bubble
c	critical
eff	effective
f	fluid
r	resistance temperature detector
Si	silicon
sat	saturated
sub	subcooled
T	temperature
w	wall

hydrodynamic property of boiling, the subcooling of working fluids confines the behavior of nucleated bubbles [21]. Specifically, NF surfaces contain submicron nucleation sites [10–12,18] that are compatible with heterogeneous ebullition under subcooling conditions, resulting in discrete nucleation and suppressed bubble development.

Although many researches into enhancing boiling heat transfer via nanoscale morphology control have been conducted [10–16],

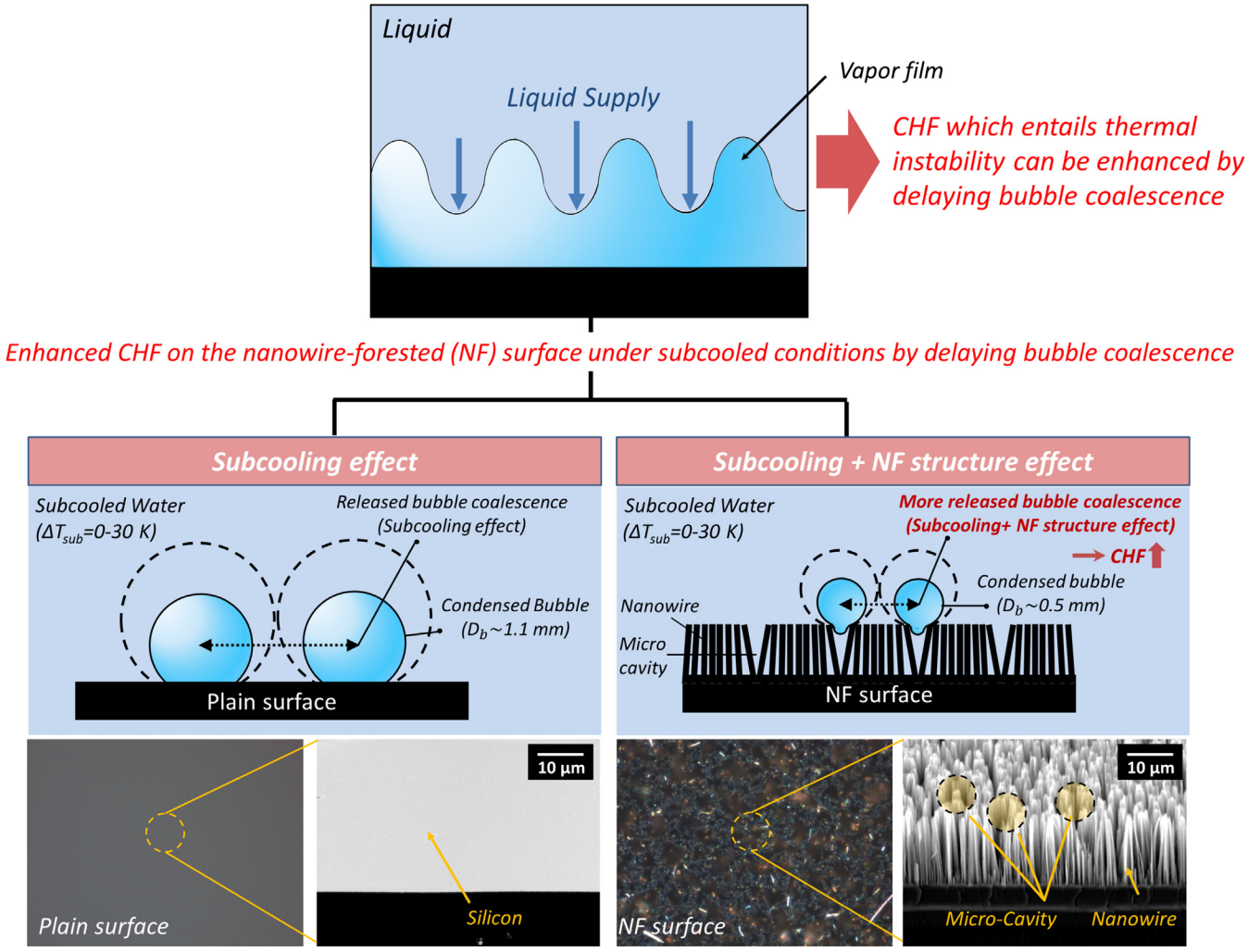

Fig. 1. Schematic diagram showing the effects of nanowire-forested (NF) structures and subcooling conditions on critical heat flux (CHF) enhancement during pool boiling heat transfer.

few researchers have investigated the combined effects of nanoscale morphology and subcooling in the context of boiling heat transfer enhancement. In this study, we demonstrate the enhancement of CHF and heat transfer uniformity/stability on NF surfaces under various subcooling conditions based on bubble nucleation mechanism using bubble visualization method. The effects of NF structures on boiling heat transfer are investigated under 0–30 K subcooling conditions using a resistance temperature detector (RTD) sensor with five measuring points. The quantitative CHF improvement on NF surfaces under subcooling conditions is correlated with the sensitivity of CHF (i.e., the rate of CHF increase per degree of subcooling). Finally, we suggest that NF surfaces can be feasibly adapted under subcooling conditions to enhance CHF via improved heat transfer stability.

2. Experimental methods

2.1. Preparation of nanowire-forested (NF) surfaces

We fabricated the nanowire surfaces using a metal-assisted chemical etching method (MaCE) [20,22,23]. Using a piranha solution (3:1 mixture of H_2SO_4:H_2O_2), the substrate was cleaned by dipping the selectively exposed RTD sensor, which was protected by a Teflon cover, into the solution for 40 min. The substrate was further cleaned in methanol for 5 min, and then acetone for 5 min. Next, the exposed area containing RTD sensor, which is on the opposite side to RTD circuits, was exposed to an etching solution (a mixture of 5-M HF and 0.02-M $AgNO_3$) at room temperature. The Ag^+ ions in the solution naturally adhered to the exposed silicon (Si) surface via an electrolytic substitution reaction. Oxidation occurred at the point of contact between the Si surface and the Ag^+ ions, followed immediately by an etching reaction with the HF. Thus, vertically aligned nanowires formed on the Si surface region that had not been etched. In this study, NF surfaces, which had an average height of 17 μm, were fabricated according to the method shown in the inset of Fig. 1. The fabricated NF surfaces contained the natural micro-scale cavities (sizes up to 1–2 μm), formed by van der Waals forces among the nanowires. In the following section, we discuss how these cavities can play the role of nucleation sites to promote active nucleate boiling [10,20].

2.2. Characterization of surface morphology and contact angle

The nanowire structures were characterized in terms of their average height and pitch using field-emission scanning electron microscopy (FE-SEM; Model JEOL-JSM-7001F, JEOL Ltd., Japan). The average diameters of the natural micro-scale cavities in NF surfaces were measured using the commercially available microscope software "I'MEASURE 2.0" (Ingplus, Korea). This software analyzes the equivalent diameter of the cavities by assuming that they are equivalent circles. The averaged equivalent diameter of the cavities was calculated by averaging the diameters from five high-resolution (2500×) SEM images. We evaluated the apparent contact angles (CAs) on plain Si and NF surfaces using a CA measurement system (KSV CAM-200, KSV Instruments, Finland). The required images were taken with a high-speed camera with a resolution of 512 × 480 pixels and a 2-ms time interval. The CAs were measured from images containing a droplet in contact with the solid surface. The droplets had a volume of 2 μL. The CA was taken to be the average of five measurements obtained under the same conditions. Some of the geometric parameters of NF surfaces, such as the roughness, CA, and average diameter, pitch, and height of the nanowires, are listed in Supplementary Information.

2.3. Pool boiling facility and experimental conditions

Fig. 2(a) is a schematic of an experimental pool-boiling apparatus consisting of a main reservoir, a test section, a data-acquisition system, and a bubble-visualization system. The bulk temperature of the working fluid in the main reservoir was controlled by two immersion heaters and a coil-type heat exchanger. The heat flux of immersion heaters was controlled by a proportional-integral-derivative (PID) controller and the coil-type heat exchanger which connected to constant temperature water bath was used for maintaining subcooling temperature of working fluid in the main reservoir. Two K-type thermocouples are installed in the reservoir (as shown in Fig. 2(a)) to measure local temperatures of a fluid and

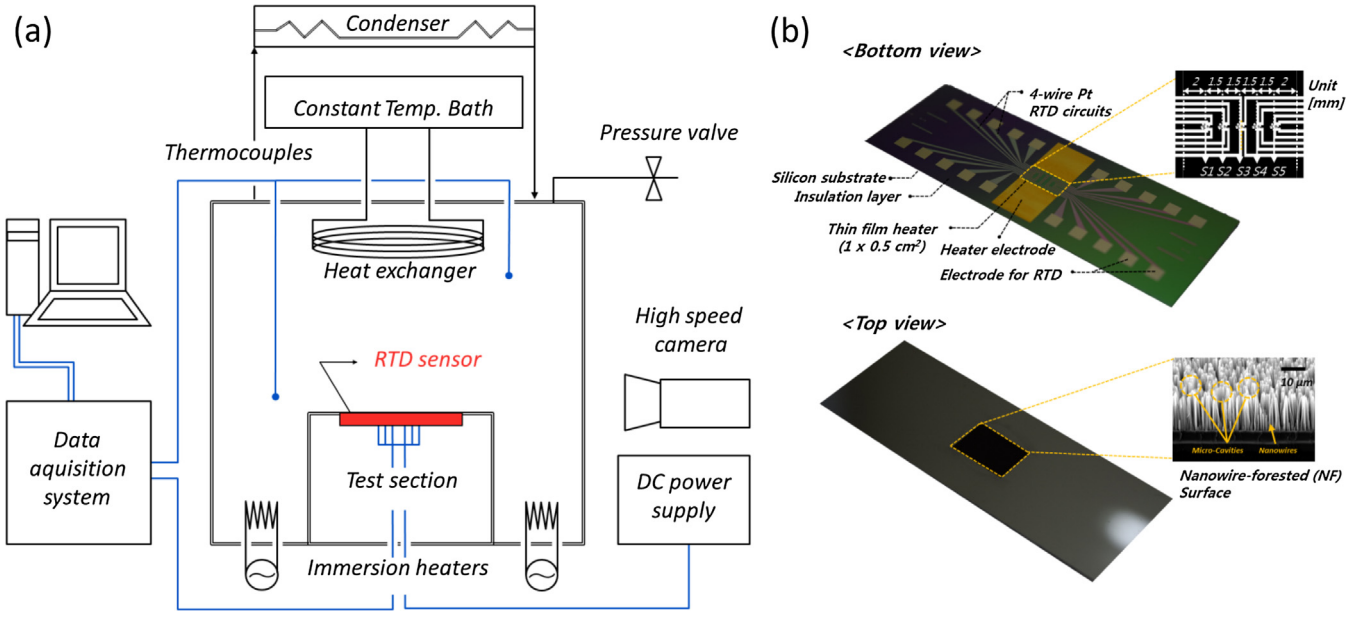

Fig. 2. Pool boiling system and resistance temperature detector (RTD) sensor. (a) Schematic diagram of the pool boiling experimental apparatus. (b) Photographs of RTD sensor with five measuring points. The five measuring points are marked S1–S5 from left to right (top) and NF structures are fabricated on the heating surface (bottom).

it was used for checking a steady condition. A pressure gauge and a vapor exhaust valve are installed to monitor and regulate pressure conditions. The transparent windows on each face of the reservoir enabled us to observe and photograph the bubbles. The test section, which is for the installation of the local-temperature-measuring RTD sensor, is located in the center of the reservoir. The body of the test section was made from Macerite ceramic (melting point: 1200 °C; thermal conductivity: 1.6 W/m·K) and polyether ether ketone (PEEK; thermal conductivity: 1.7 W/m·K). These materials were selected to minimize conductive heat loss and prevent failures, even at CHF. We connected the electric circuits used to transmit the signal from RTD sensor via a data-acquisition system and a power supply was connected to the indium tin oxide (ITO) heater on RTD sensor. The electrodes on RTD sensor were connected to the circuit by spring probes and copper bars. The power supply was used to adjust the current passing through ITO heater on RTD sensor and control the heat flux during the experiments. The data-acquisition systems analyzed the electrical resistance from RTD sensor, temperatures in the reservoir, current, and voltage-drop from ITO heater. We use deionized water as the working fluid, which was subcooled by 0, 10, 20, and 30 K under ambient pressure conditions. In order to remove dissolved gas in deionized water, degassing was conducted for 2 h prior to the experiment. We conducted boiling experiment by fully filling up the boiling chamber with the liquid to avoid the air space. In addition, we installed condenser on the top of the boiling chamber for avoiding loss of liquid, which can cause the air space of phase change phenomena, by evaporation during 2 h degassing process. Furthermore, because most of evaporated vapor changed to liquid due to the condenser at the upper side of experimental apparatus, the amount of liquid in the boiling chamber is hardly decreased during 2 h degassing process. For these reasons, the air layer is rarely generated in the chamber even after degassing. We closed the pressure valve while setting the subcooling condition. This prevented gas inflow into the chamber as the fluid temperature decreased. All experiments were conducted while the bulk fluid temperature and heat flux at the ITO heater were in a steady state. We ensured steady heat-flux conditions by monitoring the voltage drop and RTD signals for more than 3 min after each measurement and current adjustment. The sampling frequency of the surface temperature data from RTD sensor was 1000 Hz and the voltage drop and thermocouple signals were measured at a rate of 2 Hz. The data presented in this study are averaged values from a measurement period of 30 s, obtained under steady-state conditions.

2.4. Visualization of bubble behavior and characteristics

We used a high-speed camera (Speedsense M110, Dantec, Denmark) and bubble visualization imaging software (ver. 3.30, Dynamic Studio, Denmark) to acquire images of the departing bubbles, with an 80-W light-emitting diode backlight. Detailed bubble images and the methods used to evaluate the equivalent bubble departure diameters can be found in Supplementary Information.

2.5. Resistance temperature detector (RTD) sensor

RTD sensor was used for local temperature measurements and to evaluate the boiling heat transfer performance. RTD sensor consisted of a thin-film ITO heater (thickness: 500 nm) and a four wire RTD sensor with five measuring points (S1–S5). Fig. 2(b) shows RTD sensor used in this study. The distance between each measuring point was 1.5 mm, and the ITO heater with a heating area of 0.5 cm × 1.0 cm was placed at the center of RTD sensor (7.5 cm × 2.5 cm). RTD sensor enabled us to make accurate and reliable spatial and temporal surface temperature measurements on the boiling surface, as the perturbations caused by the installation process were diminished. The response time of the sensor was 2.84 ms (about 350 Hz); we intended for this to be less than the bubble departure frequency, which was on the order of tens to hundreds of hertz. RTD sensor is made of thin Pt layer (0.1 μm) and the size is 162 × 162 μm^2, so RTD sensor is capable of spatial temperature measurement. The four wire method was used for measuring the exact resistance of the serpentine design on RTD sensor. The resistance of RTD sensor is big owing to the serpentine design, and the increase in resistance due to temperature change is large enough for accurate measurements ($\Delta R/\Delta T \sim 1.5\ \Omega/°C$). Therefore, RTD sensor can have the benefits of accuracy and reliability. The details of the method used to fabricate RTD sensor are described in our previous papers [10,19,20].

2.6. Data reduction

The applied heat flux, q'', can be calculated using $q'' = V{\cdot}I/A$. Hence, q'' can evaluated by measuring the applied current, I, the voltage drop from the heater, V, and the confined heating area, A. The five temperature measurement points and the ITO heater were positioned at the bottom of RTD sensor. Therefore, we calculated the exact boiling surface temperature using $T_w = T_r - (q''{\cdot}t_{Si})/k_{Si}$ where T_w, T_r, t_{Si}, and k_{Si} are the wall temperature just on the boiling surface, the temperature measured by RTD, the thickness of the Si substrate, and the thermal conductivity of Si, respectively. As the Si substrate was thin (thickness: 500 μm), and Si has a high thermal conductivity of 140 W/m·K, we assumed that heat was conducted one-dimensionally, through the thickness of the Si substrate [10,19,20]. We determined the onset of nucleate boiling (ONB) by apparent bubble observation, and CHF by detecting temporal surface temperature fluctuations over 15 K. As we were concerned that CHF would damage the equipment, we predicted CHF as follows. The quantitative CHF value was determined by adding half of the increment between the last heat flux showing the fluctuation and the previous one prior to observing the symptom [10,19,20]. The detailed explanations for determination of CHF are contained in the Supplementary Information.

2.7. Uncertainty analysis

We predicted all errors from the experiments presented in this study with a 95% confidence level, based on measured data for each variable. Uncertainties associated with both the basic dimensional variables and the main variables obtained from the data-reduction procedure described above were analyzed using the method suggested by Moffat [24]. The errors in the dimensional estimations of RTD sensor were ±0.2% and ±1.32 K for the K-type thermocouples. The main source of error in boiling experiments was heat loss due to conduction to the test sections. It is not easy to estimate this heat loss directly; thus, we estimated it indirectly by analyzing the boundary conditions obtained from the experiments. This estimation is reflected in the uncertainty of the applied heat flux. Specifically, we used commercial CFD software (Fluent v.6.3.26, ANSYS) to estimate the heat loss numerically. We compared the numerical results to the experimental measurements of the local temperature at the center of the heating surface. Then, we conducted iterative calculations until the deviation between the numerical and experimental results was 1.0%. Once this condition was satisfied, we estimated the quantitative heat loss by comparing the heat flux outwards from the heater surface to the inward-projected heat flux. The uncertainty of the applied heat flux with this heat-loss prediction is $(\delta q''/q'') = [(\delta V/V)^2 + (\delta I/I)^2 + (\delta A/A)^2]^{1/2} + q''_{loss}$, or 6.50%. The uncertainties in the wall temperature (6.52%) and convective heat transfer coefficient (9.21%) were estimated using the same procedure. The uncertainty in the non-

dimensional Jakob number was 0.02%, and the pixel uncertainty in the bubble diameters in bubble shadow images was ±0.1 mm.

3. Results and discussion

3.1. Effects of nanowire-forested structures on boiling heat transfer under subcooling conditions

CHF occurs when bubbles merge vigorously and form a vapor film. This impedes heat dissipation from the boiling surface. To maximize CHF, it is essential to weaken or delay the coalescence of bubbles, even in high heat flux conditions [25–29]. The bubble detachment size is a crucial factor in determining bubble merging. It has been shown that there is a linear relationship between nucleation and detachment bubble size during boiling [30,31]. As we attenuate the nucleation size to decrease the bubble detachment size, the attraction between bubbles diminishes, reducing the rate of coalescence. Moreover, the vacant space between bubbles leads to favorable liquid accessibility, enabling surface rewetting during the phase change of the working fluid. Therefore, we can propose how to obtain high CHF by considering the nucleation of small bubbles. We suggest two strategies for nucleating small bubbles, as shown in Fig. 1. From the near-field hydrodynamic perspective, one strategy is to use NF structures that contain micro-cavities, which act as nucleation seeds. The near-field interfacial characteristics associated with this morphology can be controlled to manipulate the bubble nucleation behavior and confine the arising bubbles. The other strategy is based on the perspective of far-field hydrodynamics; subcooling the working fluid shrinks the bubbles generated. Fewer confined and shrunken bubbles coalesce, preventing the formation of the insulating vapor film at high heat flux.

CHF was 115% greater on NF surfaces than on plain surfaces at the saturated fluid temperature, as shown in Fig. 3. The enhanced CHF on NF surfaces demonstrates that the morphological features of NF surfaces promote boiling by offering nucleation sites in the form of submicron cavity-like structures, and by preserving superhydrophilic characteristics with strong interfacial hemi-wicking [12,19,20]. NF surfaces have strong hydrophilic wetting characteristics, with a CA below 10° (Fig. 3, inset). As shown in Fig. 4(a), the average bubble departure diameter depends on the presence of nanostructures, and decreases from 2.96 mm on plain surfaces to 1.10 mm on NF surfaces at the saturated fluid temperature. In addition, as shown in Fig. 4(b), the average bubble departure frequency increased from 41 Hz on plain surfaces to 74 Hz on NF surfaces at the saturated fluid temperature. Separately detaching small bubbles with a high detaching frequency leads to the creation of large vacant spaces between bubbles. This allows the liq-

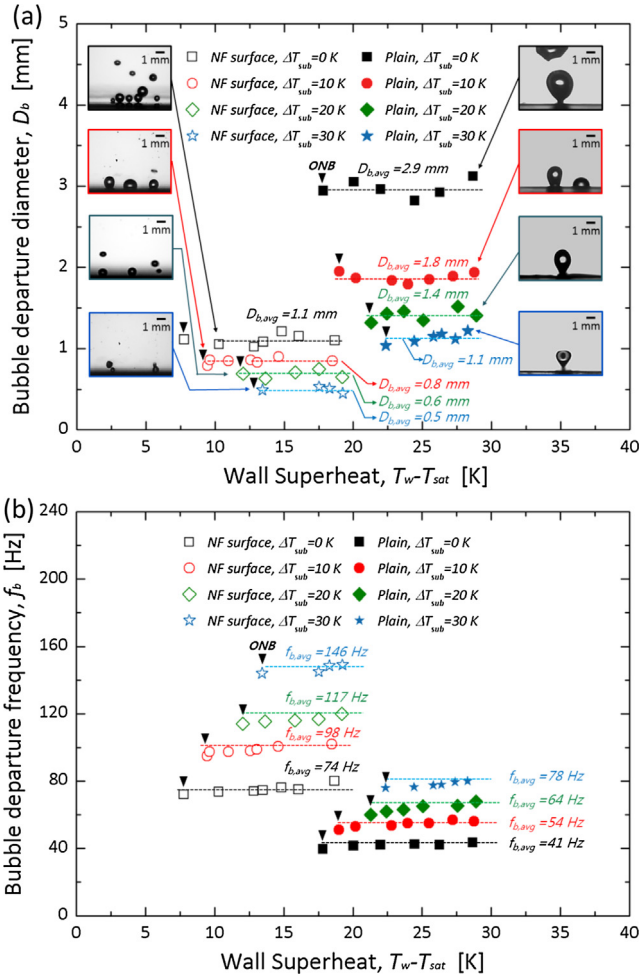

Fig. 4. Bubble departure characteristics on plain and NF surfaces under subcooling conditions. Black reversed triangles indicate ONB. The Inset shows the images of bubble departure characteristics, averaged bubble departure diameter and frequency, respectively. (a) Averaged bubble departure diameters. (b) Averaged bubble departure frequencies.

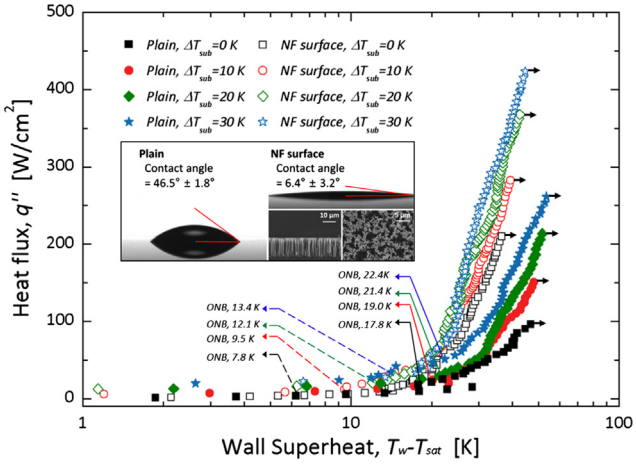

Fig. 3. Boiling curves on plain and NF surfaces. Black arrows indicate CHF. Insets present static wetting characteristics, SEM images of NF surfaces and wall superheat of onset of nucleate boiling (ONB), respectively.

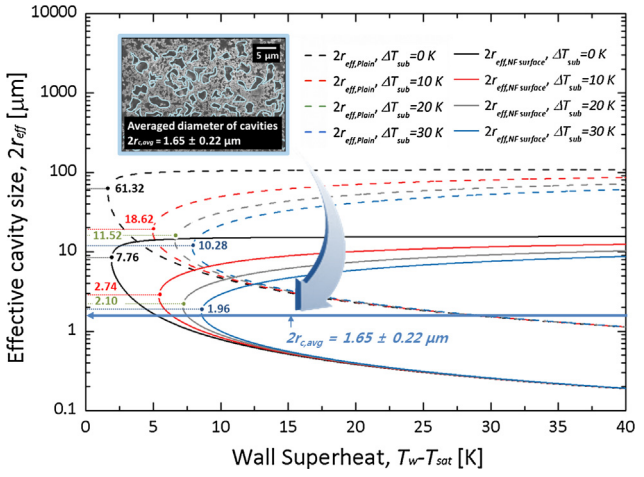

Fig. 5. Effective cavity diameter ranges of plain and NF surfaces under subcooling conditions. The inset SEM image shows the micron-scale cavity-like structures formed by the conglomeration of nanowires.

uid to access the boiling surface directly. These are intrinsic characteristics of NF surfaces that effect ebullition behavior in a manner that improves CHF [18].

In light of bubble formation and coalescence, as an ideal far-field factor in boiling, the subcooling condition is controlled to attenuate vigorous bubble generation and suppress its coalescence. The thermal boundary layer created by superheating a fluid near a boiling surface supports the development of bubbles. The thickness of the thermal boundary layer is inversely related to the degree of subcooling. That is, subcooling accompanies a decrease in the thermal energy supplied to the fluid for bubble development. Consequently, it confines unlimited bubble growth by configuring the temperature gradient from a boiling surface, which accompanies local superheating of a fluid over a boiling point, to subcooled bulk fluid. Moreover, after their departure from the boiling surface, bubbles condense in the subcooled bulk fluid. The condensation at the interface between the liquid and the bubble is proportional to the level of subcooling [21]. Bubble departure diameters are shown in Fig. 4(a); on plain surfaces, the bubble departure size decreased from 2.96 mm (w/o subcooling) to 1.13 mm (with 30 K subcooling) as the level of subcooling increased. Bubble departure frequency increased with the level of subcooling, from 41 Hz to 78 Hz on plain surfaces, as shown in Fig. 4(b). The bubble departure frequency mostly depends on the bubble waiting period, because the waiting period is much longer than the growth period [32,33]. The waiting period is defined as the time it takes for the thermal boundary layer to recover after a bubble departs from the nucleation site. It was recently reported that the recovery of the thermal boundary layer is governed by a combination of transient conductive and convective heat transfer in the case of highly subcooled liquids ($\Delta T > 5$ K) [32,33]. The thermal boundary layer recovers faster in the high subcooling case because there is a large temperature gradient and, hence, higher convection, compared with the saturated condition. This mechanism can be used to

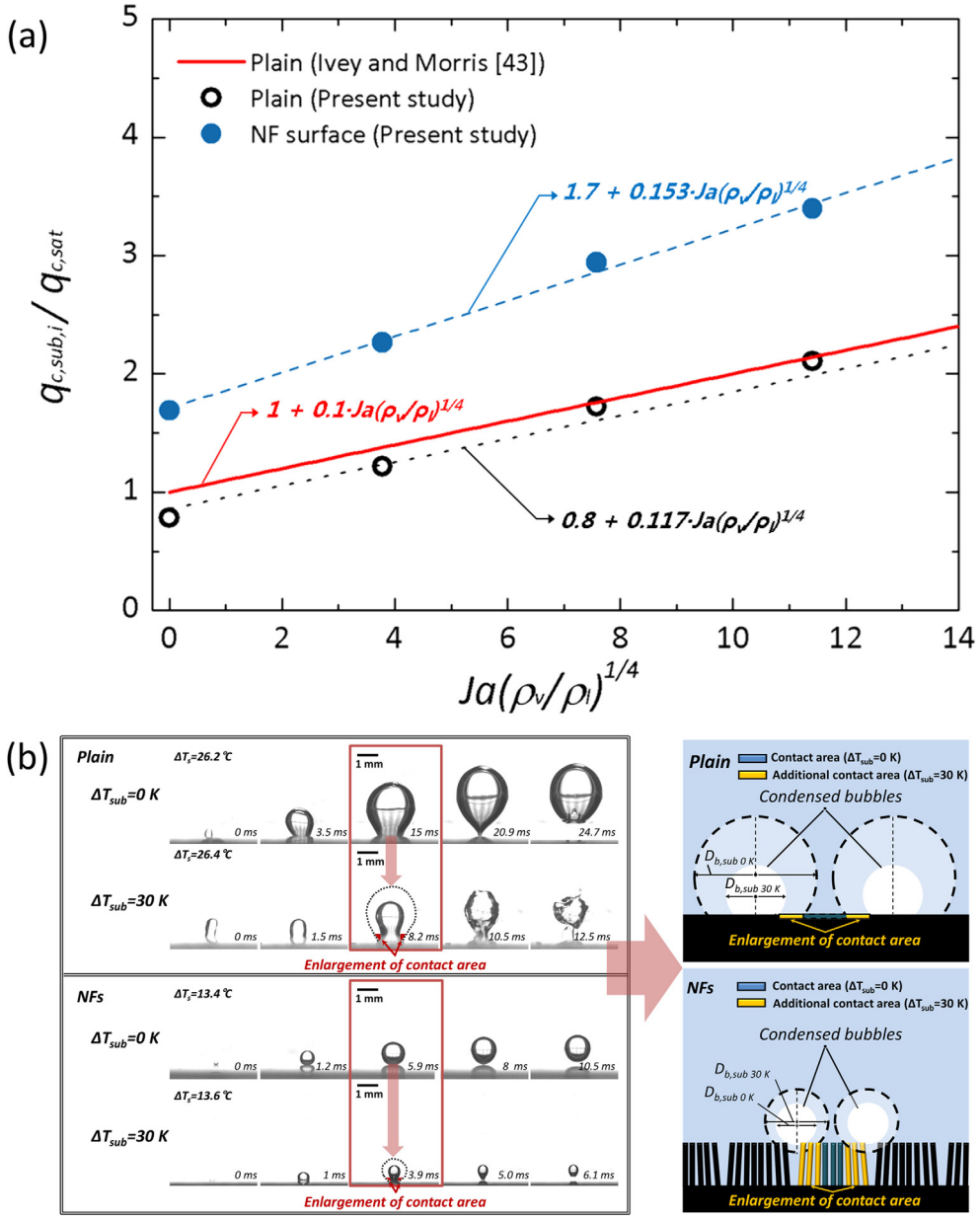

Fig. 6. (a) CHF sensitivity as a function of the Jakob number (degree of subcooling) and surface manipulation [43]. (b) Photographs of nucleation dynamics (left) and schematic diagram of its effect on the CHF sensitivity (right) of plain and NF surfaces.

reduce the waiting period and increase the bubble departure frequency for liquids that are subcooled by more than 5 K. The smaller and faster bubble detachment promotes liquid accessibility by introducing vacant areas. These are required to ensure hydrodynamic stability between the upward bubble escape and downward liquid refresh under subcooled conditions. Fig. 3 shows that 30 K subcooling improved CHF by more than 168% on untreated plain surfaces.

Considering the aforementioned independent strategies of manipulating the near-field morphological interface using a surface with NF structures and introducing far-field hydrodynamic effects by subcooling, a possible synergetic effect can be pursued for higher CHF. Suppression of bubble development under subcooling could be optimized on manipulated NF surfaces, which promotes smaller and easier nucleation of bubbles with lower wall superheating through their own cavity-like nucleation sites. Fig. 4(a) shows that the smallest bubbles—with diameters of up to 500 μm—occur even at the detaching stage on NF surfaces with 30 K subcooling. This can be explained from the bubbles' origin of nucleation according to effective cavity sizes. As discussed, the bubble departure should rely on their nucleation and sequential development determined by morphological characteristics and thermohydrodynamic conditions above a boiling surface [12,20]. Regarding these points, the prerequisite condition for nucleation can be demonstrated by considering embryo evolution into bubble nucleation [10,30,31]. For active nucleation sites, vapor nuclei should form at an elevated pressure that is higher than that of the surrounding liquid. The pressure difference between the nuclei and the surrounding liquid is $\Delta P = 2\gamma/r_b$ where γ and r_b are the surface tension of the fluid and the radius of the bubble, respectively. Herein, wall superheating is an apparent energy source for the pressure increase, and it induces a temperature gradient in the thermal boundary layer. In the presence of wall superheating and a subcooled bulk fluid, the range of effective nucleation cavities r_{eff} is predicted as follows [31]:

$$\left\{ \begin{matrix} r_{\mathrm{eff,min}}(\Delta T_w, \Delta T_{\mathrm{sub}}) \\ r_{\mathrm{eff,max}}(\Delta T_w, \Delta T_{\mathrm{sub}}) \end{matrix} \right\} = \frac{\delta D_2}{2D_1} \cdot \frac{\Delta T_w}{\Delta T_w + \Delta T_{\mathrm{sub}}} \left[1 \left\{ \begin{matrix} - \\ + \end{matrix} \right\} \sqrt{1 - \frac{8D_1 \gamma T_{\mathrm{sat}}(P_l)(\Delta T_w + \Delta T_{\mathrm{sub}})}{\rho_v l \delta_t (\Delta T_w)^2}} \right], \quad (1)$$

where ΔT_w, ΔT_{sub}, δ, T_{sat}, ρ_v, and l are the wall superheat, degree of subcooling, thermal boundary layer thickness, liquid saturation temperature, vapor density, and latent heat of the fluid, respectively. The static wetting characteristics of an interface are reflected by two terms: D_1 (= 1 + cosθ) and D_2 (= sinθ) where θ is the apparent CA on the interface. The effective cavity diameter $2r_{eff}$ is governed by both the wetting (θ is 46.5° and 6.4° on plain and NF surfaces) and subcooling, as shown in Fig. 5. Hence, we can reduce r_{eff} by increasing the level of subcooling. In particular, $2r_{eff}$ decreased from 7.76 μm to 1.96 μm on NF surfaces when we increased the degree of subcooling to 30 K. To understand the synergetic effects of NF surfaces under subcooling, we focus on several interesting characteristics of NF surfaces: 17-μm-high NF surfaces create cavity-like structures formed by their conglomeration due to the van der Waals force [20,22,23] and their averaged characteristic diameter 2rc,avg is approximately 1.65 ± 0.22 μm as shown in the inset of Fig. 5, which readily realize small nucleation commensurate with the effective cavity predictions in Fig. 5. NF structures-created cavities with a characteristic diameter near $2r_{eff}$ must be effective to catalyze nucleation with lower wall superheat. Since the excellent match-up between the apparent characteristic size and the prerequisite of effective cavities is attained by the manipulation of an interface, the smallest bubbles could be monitored on NF surfaces with 30 K subcooling. Bubble departure sizes are much smaller and bubble coalescence is more suppressed on NF surfaces compared to plain surfaces under the 30 K subcooling condition at various wall superheat. The integrative approach of the far-field subcooling control and the near-field surface manipulation could lead to CHF extension.

3.2. Sensitivity of CHF on NF surfaces under subcooling conditions

CHF sensitivity under subcooling refers to the dependency of CHF enhancement on subcooling. It is clear that NF surfaces are optimal candidates for enhancing CHF under subcooling conditions [16,25,34–41]. CHF is expressed directly in terms of the degree of subcooling. The secondary effects on local convective behavior can be described in terms of properties that depend on pressure. At atmospheric pressure, CHF improvement is expressed as $q_{c,sub}/q_{c,sat} \sim 1 + f(\Delta T_{sub},\ \rho_l(P)/\rho_v(P))$ [4,38,41]. In the case of untreated plain surfaces with no interfacial manipulations, subcooling has no effect on CHF sensitivity, which implies the absence of interfacial effects. Thus, we can derive a modified expression for CHF ratio that considers the effects of both subcooling and interfacial modifications, as follows:

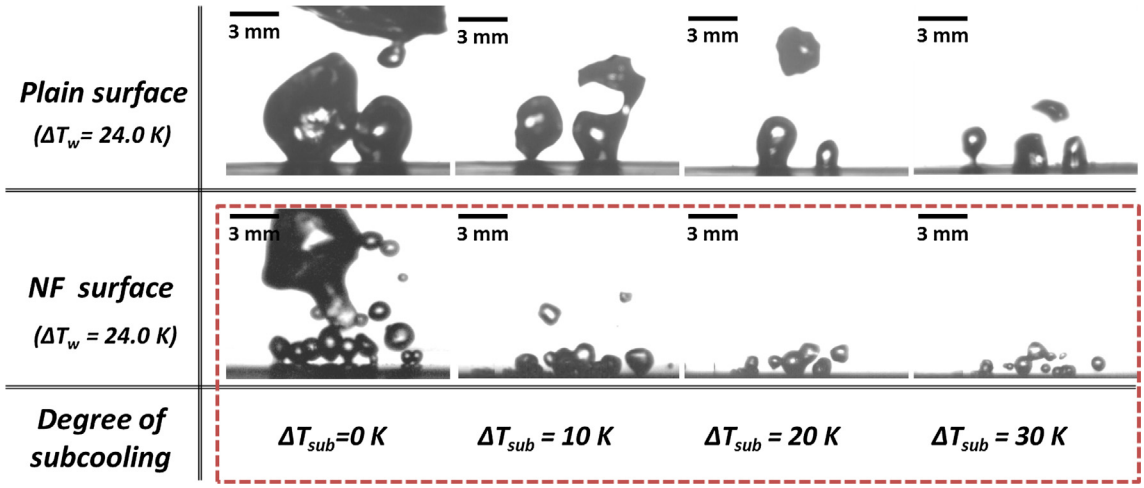

Fig. 7. Shadowgraph images of bubbles at the same wall superheat temperature under subcooling conditions on plain and NF surfaces. The red dotted box describes the bubble departure characteristics of NF surfaces under different subcooling conditions. (For interpretation of the references to color in this figure legend, the reader is referred to the web version of this article.)

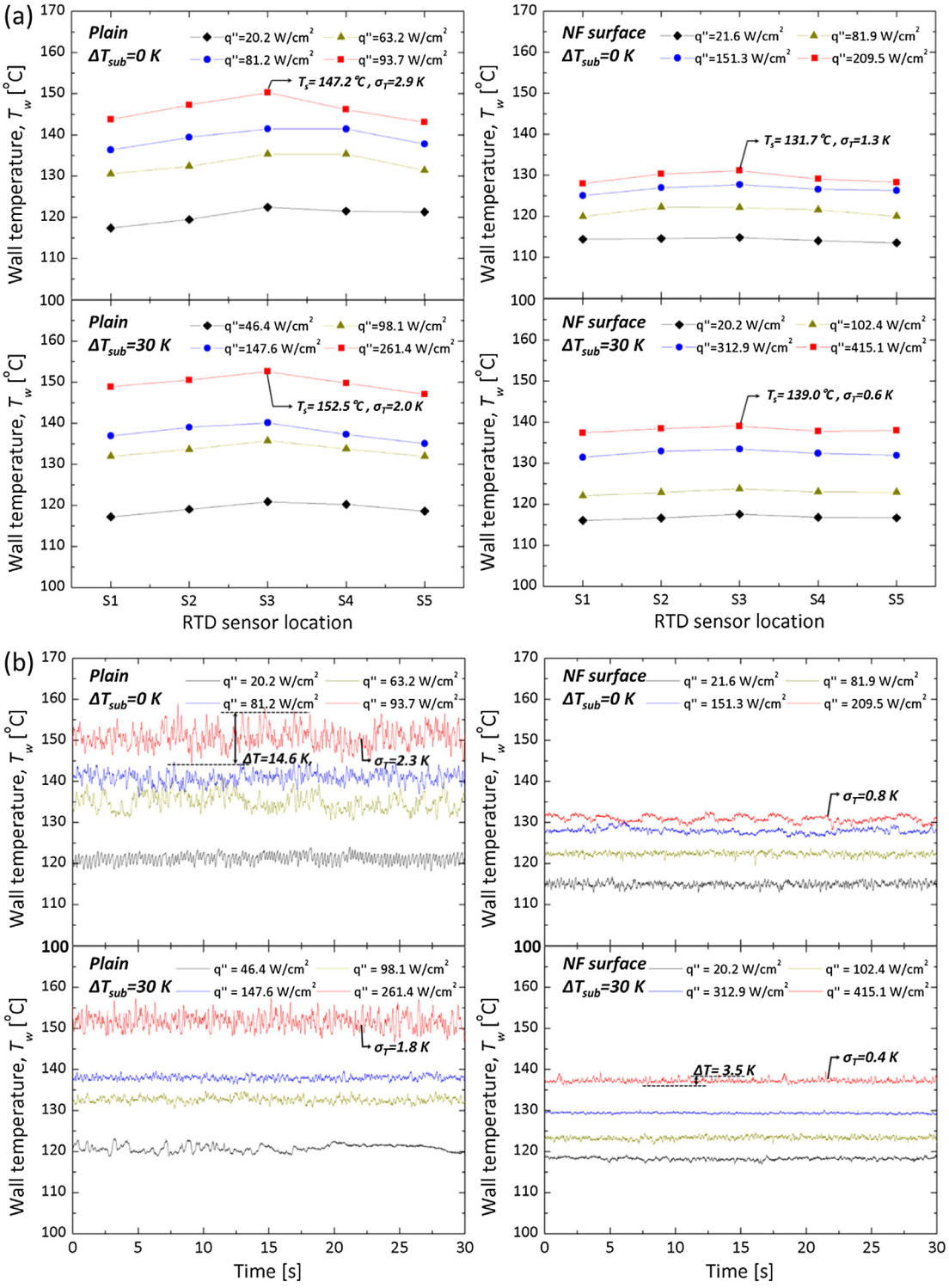

Fig. 8. Thermal uniformity and stability of plain and NF surfaces under 0 K- and 30 K-subcooling conditions for various heat flux values. (a) Temperature distribution (RTD sensor locations: S1–S5) and (b) temperature variation with time (at RTD sensor location S3) on plain and NF surfaces under 0 K- and 30 K-subcooling conditions.

$$\frac{q_{c,\mathrm{sub},i}}{q_{c,\mathrm{sat}}} = \left(\frac{q_{c,i}}{q_c}\right)_{\mathrm{sat}} + f\left(\Delta T_{\mathrm{sub}}, \frac{\rho_l(P)}{\rho_v(P)}\right) = A_i + S_i \cdot \left(\frac{\rho_l}{\rho_v}\right)^{-\frac{1}{4}} \cdot Ja \quad \left(Ja = \frac{\rho_v}{\rho_l} \cdot \frac{C_p \cdot \Delta T_{\mathrm{sub}}}{l}\right), \tag{2}$$

where Ja, C_p, ρ_v, ρ_l and l are the Jakob number, the specific heat of the liquid, the density of the vapor, the density of the liquid and the latent heat of the liquid, respectively. The subscript i denotes the surface condition. A_i is the ratio of CHF on the manipulated surface to CHF on an untreated surface at saturation. This indicates the advantages of surface manipulation even at saturation. S_i is CHF sensitivity under subcooling, which represents the gradient of CHF increment versus subcooling. Herein, Zuber's CHF model is used to predict a reference CHF at saturation that takes the effect of pressure into account [25,42]. We can see from Fig. 6(a) [43] that

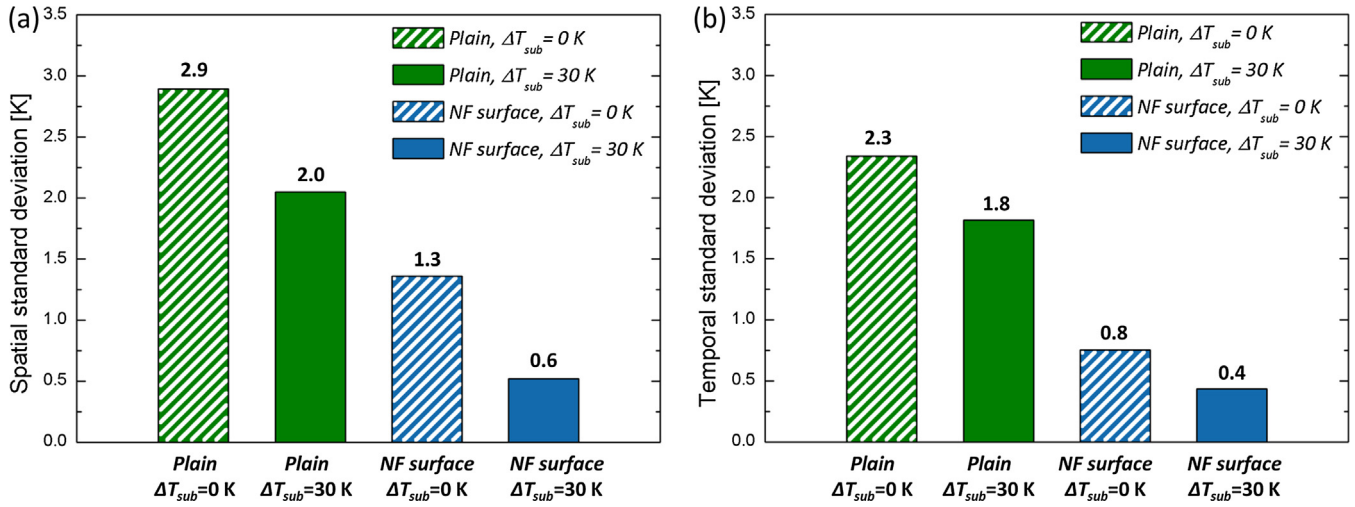

Fig. 9. (a) Standard deviation of the surface temperature (RTD sensor locations: S1–S5) and (b) standard deviation of the temporal temperature variation (at RTD sensor location S3) at CHF on plain and NF surfaces under 0 K- and 30 K-subcooling conditions.

the interfacial effects induced by NF structures benefit both the y-intersect, A_i, which is 115% larger than that of plain surfaces, and the sensitivity, which increased by 30.8%. The increase in A_i induced by the nanoscale structures can be explained in terms of near-field effects. The improvement is caused by the intrinsic interfacial characteristics of direct interfacial re-wetting and hemi-wicking, which is attributed to the rough morphology on a high surface energy substrate [18–20]. Thus, the catalytic cavity-like structures enhanced sensitivity, which was further optimized by subcooling under nucleation-suppression conditions. The sensitivity improvement may be caused by a synergetic effect. Liquid accessibility is required to delay CHF onset; nucleation and the resulting surface rewetting are enhanced by subcooling, which diminishes bubble nucleation/development. While the subcooling reduces the sizes of the bubbles on the boiling surface, the direct contact area between the heat-transfer surface and the bulk liquid is enlarged, increasing the number of heat-dissipation paths. The visualized bubble images in the red[2] square of Fig. 6(b) show the effect of subcooling on bubble size and the enlargement of the liquid contact area on plain and NF surfaces. Both images in the red square were photographed at the end of the inertia-controlled growth period, which means that the bubble contact area was maximized during bubble growth and departure [37]. As opposed to plain surfaces, the extension of the vacant solid–liquid contact area leads to additional hemi-wicking, which promotes liquid accessibility on NF surfaces. The contact area increases more on surfaces with higher interfacial roughness, such as NF surfaces, than on lower-roughness or untreated surfaces, as shown in Fig. 6(b). Therefore, CHF sensitivity, which depends on the level of subcooling, is a function of the morphology of the interface. It can be improved using highly roughened boiling surfaces, as these cause severe bubble shrinkage and ebullition. CHF sensitivity of NF surfaces is 0.153, 30.8% greater than that of plain surfaces (S_{plain} = 0.117). Although the scope for making quantitative comparisons with the results of previous work is limited due to the differences in experimental conditions and fluidic properties, the sensitivity enhancement of up to 30.8% on NF surface is a remarkable achievement compared with the 13% increase resulting from manipulating the morphology of micro-porous structures [44]. This highlights the validity of the role of NF surfaces, which can be optimized with subcooled boiling, compared with other types of manipulated surfaces.

[2] For interpretation of color in Fig. 6, the reader is referred to the web version of this article.

3.3. Thermal uniformity and stability on NF surfaces under subcooling conditions

As shown in Fig. 7, NF surfaces in subcooling conditions generate even smaller and faster bubbles than saturated NF surfaces, resulting in better temperature uniformity/stability under subcooling conditions. Fig. 8(a) shows the time-averaged spatial temperature distribution (RTD sensor locations: S1–S5) of the boiling surface on plain and NF surfaces under subcooling temperatures of 0 K and 30 K. There were large local temperature deviations on the plain surfaces, over 7.2 K over the short lateral distance (3 mm) from the center of RTD sensor to the outer edge. In the saturated condition, the temperature at the center exceeded 147.2 °C with a spatial standard deviation of 2.9 K at a heat flux of 93.7 W/cm^2. In contrast to the plain surfaces, the temperature at the center of NF surfaces decreased remarkably, to 131.7 °C, the spatial standard deviation decreased to 1.3 K, and the heat flux was 209.5 W/cm^2 under saturated conditions. Additionally, temperature uniformity was enhanced by immersing NF surfaces in highly subcooled water (ΔT_{sub} = 30 K), leading to a spatial standard deviation of 0.6 K and heat flux of 415.1 W/cm^2. From these results, we can conclude that NF surfaces with high subcooling (ΔT_{sub} = 30 K) exhibit enhanced surface temperature uniformity, with a spatial standard deviation of less than 0.6 K. Fig. 8(b) shows the temporal variations of the surface temperature at the central point (S3) of the plain and NF surfaces under subcooling temperatures of 0 K and 30 K. On the plain surfaces, the amplitude of the peak temperature fluctuations was greater than 14.6 K, the temporal standard deviation was 2.3 K, and the heat flux was 93.7 W/cm^2 in saturated conditions. These high temperature fluctuations occurred because the coalescing bubbles formed a vapor film that limited heat dissipation towards the working fluid. This phenomenon generates sudden temperature increases that eventually cause thermal failures at the surface. Severe temperature fluctuations can create a large temperature gradient on the boiling surface, which leads to high thermal stress. Recurrent thermal stress under long-term boiling applications causes thermal fatigue and, eventually, critical thermal failure. In contrast to the plain surfaces, no abnormal temperature fluctuations occurred on NF surfaces for any of the heat flux or subcooling conditions tested. The temporal standard deviation was 0.8 K and the heat flux was 209.5 W/cm^2 on NF surfaces under saturated conditions. In addition, we significantly reduced the amplitude of the temperature fluctuations by immersing NF surfaces in highly subcooled water (ΔT_{sub} = 30 K). In this case, the

amplitude of the temperature fluctuations was less than 3.5 K, the temporal standard deviation was 0.4 K, and the heat flux was 415.1 W/cm^2.

In summary, as shown in Fig. 9(a) and (b), using saturated NF surfaces to enhance temperature uniformity/stability, we reduced the spatial and temporal standard deviations of the temperature at CHF from 2.9 K to 1.3 K and 2.3 K to 0.8 K, respectively. When combining NF surfaces with high subcooling (ΔT_{sub} = 30 K), we reduced the spatial and temporal standard deviations of the temperature at CHF from 1.3 K to 0.6 K and from 0.8 K to 0.4 K, respectively. This is because NF surfaces under subcooling conditions generate smaller bubbles with a higher departure frequency than saturated NF surfaces. As a result, large spatial/temporal vacant areas form between the bubbles, permitting direct contact between the boiling surface and the working fluid. These physical explanations of the spatial/temporal bubble dynamics, which increase the liquid re-wetting capability, may be the primary cause of the reduced spatial/temporal temperature deviations of NF surfaces under subcooling conditions. In other words, we have demonstrated that NF surfaces under the subcooling conditions significantly enhance the heat transfer uniformity/stability. We reduced the spatial/temporal temperature variations, on NF surfaces with 30 K subcooling, to less than 1/5 of that on plain surfaces under the saturated condition. This highlights the fact that we can improve thermal stability under vigorous boiling conditions using NF boiling surfaces.

4. Conclusion

We suggest that NF surfaces are efficient on boiling heat transfer under subcooling environments owing to their interfacial advantages: morphological aspects involving cavity-like nucleation sites formed by high-aspect-ratio nanostructures, and secondary hydrodynamic aspects involving bubble shrinkage and vacant area for liquid accessibility. Although subcooling of the working fluid confines the development of nucleation, NF surfaces interestingly offer sub-micron nucleation sites which can promote heterogeneous ebullition even under the subcooled conditions. Dispersed, confined and fast bubble ebullitions on NF surfaces under subcooled conditions lead to the enhancement of CHF accompanying stabilized spatial/temporal surface temperature variations by suppressing the bubble coalescences. NF surfaces applying 30 K subcooled condition remarkably diminish the spatial/temporal temperature variations at CHF to less than 1/5 of that on plain surfaces under the saturated condition. CHF of 428 W/cm^2 is obtained on NF surfaces under 30 K subcooled condition, improved by 430% compared to plain surfaces under the saturated condition. This remarkable enhancement shows that NF surfaces can be used to improve thermal stability under vigorous boiling conditions. The foregoing demonstrations and results will aid the thermal and fluidic design for micro-device [4–53] and macro-system [54–56] cooling, with applications ranging from CPU chip cooling to power-plant system cooling under severe subcooling conditions.

Conflicts of interest statement

The authors declared that there is no conflict of interest.

Acknowledgement

This work was supported by the Center for Advanced MetaMaterials (CAMM) funded by the Ministry of Science, ICT and Future Planning as Global Frontier Project (CAMM-No. NRF2014M3A6B3063716) and the Human Resources Development program (No. 20174030201720) of the Korea Institute of Energy Technology Evaluation and Planning (KETEP), grant funded by the Korea government Ministry of Trade, Industry and Energy.

Appendix A. Supplementary material

Supplementary data associated with this article can be found, in the online version, at https://doi.org/10.1016/j.ijheatmasstransfer.2017.12.100.

References

[1] G. Ghibaudo, H. Jaouen, G. Kamarinos, Integration density limitation in 3D integrated circuits due to heat dissipation, EPL 2 (1986) 209.
[2] N.S. Dhillon, J. Buongiorno, K.K. Varanasi, Critical heat flux maxima during boiling crisis on textured surfaces, Nat. Commun. 6 (2015).
[3] H.J. Cho, J.P. Mizerak, E.N. Wang, Turning bubbles on and off during boiling using charged surfactants, Nat. Commun. 6 (2015).
[4] C.-H. Choi, M. David, Z. Gao, A. Chang, M. Allen, H. Wang, et al., Large-scale generation of patterned bubble arrays on printed bi-functional boiling surfaces, Sci. Rep. 6 (2016).
[5] K.-H. Chu, R. Enright, E.N. Wang, Structured surfaces for enhanced pool boiling heat transfer, Appl. Phys. Lett. 100 (2012) 241603.
[6] H. Jo, D.I. Yu, H. Noh, H.S. Park, M.H. Kim, Boiling on spatially controlled heterogeneous surfaces: wettability patterns on microstructures, Appl. Phys. Lett. 106 (2015) 181602.
[7] D.E. Kim, S.C. Park, D.I. Yu, M.H. Kim, H.S. Ahn, Enhanced critical heat flux by capillary driven liquid flow on the well-designed surface, Appl. Phys. Lett. 107 (2015) 023903.
[8] H. O'Hanley, C. Coyle, J. Buongiorno, T. McKrell, L.-W. Hu, M. Rubner, et al., Separate effects of surface roughness, wettability, and porosity on the boiling critical heat flux, Appl. Phys. Lett. 103 (2013) 024102.
[9] S. You, T.W. Simon, A. Bar-Cohen, A technique for enhancing boiling heat transfer with application to cooling of electronic equipment, IEEE Trans. Compon. Hybr. Manuf. Technol. 15 (1992) 823–831.
[10] S. Shin, B.S. Kim, G. Choi, H. Lee, H.H. Cho, Double-templated electrodeposition: simple fabrication of micro-nano hybrid structure by electrodeposition for efficient boiling heat transfer, Appl. Phys. Lett. 101 (2012) 251909.
[11] S. Shin, T.T. Al-Housseiny, B.S. Kim, H.H. Cho, H.A. Stone, The race of nanowires: morphological instabilities and a control strategy, Nano Lett. 14 (2014) 4395–4399.
[12] C. Li, Z. Wang, P.I. Wang, Y. Peles, N. Koratkar, G.P. Peterson, Nanostructured copper interfaces for enhanced boiling, Small 4 (2008) 1084–1088.
[13] H.S. Ahn, J.M. Kim, C. Park, J.-W. Jang, J.S. Lee, H. Kim, et al., A novel role of three dimensional graphene foam to prevent heater failure during boiling, Sci. Rep. 3 (2013).
[14] L. Dong, X. Quan, P. Cheng, An experimental investigation of enhanced pool boiling heat transfer from surfaces with micro/nano-structures, Int. J. Heat Mass Transf. 71 (2014) 189–196.
[15] E. Demir, T. Izci, A.S. Alagoz, T. Karabacak, A. Koşar, Effect of silicon nanorod length on horizontal nanostructured plates in pool boiling heat transfer with water, Int. J. Therm. Sci. 82 (2014) 111–121.
[16] Y. Tang, B. Tang, Q. Li, J. Qing, L. Lu, K. Chen, Pool-boiling enhancement by novel metallic nanoporous surface, Exp. Therm. Fluid Sci. 44 (2013) 194–198.
[17] H.S. Ahn, H.J. Jo, S.H. Kang, M.H. Kim, Effect of liquid spreading due to nano/microstructures on the critical heat flux during pool boiling, Appl. Phys. Lett. 98 (2011) 071908.
[18] R. Chen, M.C. Lu, V. Srinivasan, Z. Wang, H.H. Cho, A. Majumdar, Nanowires for enhanced boiling heat transfer, Nano Lett. 9 (2009) 548–553.
[19] B.S. Kim, H. Lee, S. Shin, G. Choi, H.H. Cho, Interfacial wicking dynamics and its impact on critical heat flux of boiling heat transfer, Appl. Phys. Lett. 105 (2014) 191601.
[20] B.S. Kim, S. Shin, D. Lee, G. Choi, H. Lee, K.M. Kim, et al., Stable and uniform heat dissipation by nucleate-catalytic nanowires for boiling heat transfer, Int. J. Heat Mass Transf. 70 (2014) 23–32.
[21] R. Ahmadi, T. Ueno, T. Okawa, Bubble dynamics at boiling incipience in subcooled upward flow boiling, Int. J. Heat Mass Transf. 55 (2012) 488–497.
[22] B.S. Kim, S. Shin, S.J. Shin, K.M. Kim, H.H. Cho, Micro-nano hybrid structures with manipulated wettability using a two-step silicon etching on a large area, Nanoscale Res. Lett. 6 (2011) 1–10.
[23] B.S. Kim, S. Shin, S.J. Shin, K.M. Kim, H.H. Cho, Control of superhydrophilicity/superhydrophobicity using silicon nanowires via electroless etching method and fluorine carbon coatings, Langmuir 27 (2011) 10148–10156.
[24] R.J. Moffat, Describing the uncertainties in experimental results, Exp. Therm. Fluid Sci. 1 (1988) 3–17.
[25] J. O'Connor, S. You, J. Chang, Gas-saturated pool boiling heat transfer from smooth and microporous surfaces in FC-72, J. Heat Transf. 118 (1996) 662–667.
[26] M.M. Rahman, J. Pollack, M. McCarthy, Increasing boiling heat transfer using low conductivity materials, Sci. Rep. 5 (2015).

[27] S.G. Kandlikar, Controlling bubble motion over heated surface through evaporation momentum force to enhance pool boiling heat transfer, Appl. Phys. Lett. 102 (2013) 051611.
[28] M.Q. Raza, N. Kumar, R. Raj, Surfactants for bubble removal against buoyancy, Sci. Rep. 6 (2016).
[29] C. Hsu, W. Chiu, L. Kuo, P. Chen, Reversed boiling curve phenomenon on surfaces with interlaced wettability, AIP Adv. 4 (2014) 107110.
[30] R. Rammig, R. Weiss, Growth of vapour bubbles from artificial nucleation sites, Cryogenics 31 (1991) 64–69.
[31] N. Basu, G.R. Warrier, V.K. Dhir, Onset of nucleate boiling and active nucleation site density during subcooled flow boiling, J. Heat Transf. 124 (2002) 717.
[32] P. Goel, A.K. Nayak, P.P. Kulkarni, J.B. Joshi, Experimental study on bubble departure characteristics in subcooled nucleate pool boiling, Int. J. Multiph. Flow 89 (2017) 163–176.
[33] F. Demiray, J. Kim, Microscale heat transfer measurements during pool boiling of FC-72: effect of subcooling, Int. J. Heat Mass Transf 47 (2004) 3257–3268.
[34] A. Zou, A. Chanana, A. Agrawal, P.C. Wayner Jr., S.C. Maroo, Steady state vapor bubble in pool boiling, Sci. Rep. 6 (2016).
[35] J. Kim, Review of nucleate pool boiling bubble heat transfer mechanisms, Int. J. Multiph. Flow 35 (2009) 1067–1076.
[36] Y. Im, Y. Joshi, C. Dietz, S.S. Lee, Enhanced boiling of a dielectric liquid on copper nanowire surfaces, Int. J. Micro-Nano Scale Transp. 1 (2010) 79–96.
[37] S.M. Kwark, M. Amaya, R. Kumar, G. Moreno, S.M. You, Effects of pressure, orientation, and heater size on pool boiling of water with nanocoated heaters, Int. J. Heat Mass Transf. 53 (2010) 5199–5208.
[38] J.L. Parker, M.S. El-Genk, Enhanced saturation and subcooled boiling of FC-72 dielectric liquid, Int. J. Heat Mass Transf. 48 (2005) 3736–3752.
[39] H. Honda, H. Takamastu, J. Wei, Enhanced boiling of FC-72 on silicon chips with micro-pin-fins and submicron-scale roughness, J. Heat Transf. 124 (2002) 383–390.
[40] J.J. Wei, H. Honda, Effects of fin geometry on boiling heat transfer from silicon chips with micro-pin-fins immersed in FC-72, Int. J. Heat Mass Transf. 46 (2003) 4059–4070.
[41] Y. Elkassabgi, J. Lienhard, Influences of subcooling on burnout of horizontal cylindrical heaters, J. Heat Transf. 110 (1988) 479–486.
[42] N. Zuber, Hydrodynamic Aspects of Boiling Heat Transfer (Thesis), California. Univ., Los Angeles; and Ramo-Wooldridge Corp., Los Angeles, 1959.
[43] H. Ivey, D. Morris, On the relevance of the vapour-liquid exchange mechanism for sub-cooled boiling heat transfer at high pressure: reactor development division, Atom. Energy Establish. (1962).
[44] J. Xu, X. Ji, W. Zhang, G. Liu, Pool boiling heat transfer of ultra-light copper foam with open cells, Int. J. Multiph. Flow 34 (2008) 1008–1022.
[45] B.S. Kim, G.M. Yang, S. Shin, G. Choi, H.H. Cho, Local nucleation propagation on heat transfer uniformity during subcooled convective boiling, Heat Mass Transf. 51 (2015) 1–9.
[46] Y. Wang, S. Chung, J. Leonard, S. Cho, T. Phuoc, Y. Soong, et al., Cooling performance of nanofluids in a microchannel heat sink, in: ASME 2009 Second International Conference on Micro/Nanoscale Heat and Mass Transfer, American Society of Mechanical Engineers, 2009, pp. 617–623.
[47] Z. Wu, B. Sundén, On further enhancement of single-phase and flow boiling heat transfer in micro/minichannels, Renew. Sust. Energy Rev. 40 (2014) 11–27.
[48] S. Shin, G. Choi, B.S. Kim, H.H. Cho, Flow boiling heat transfer on nanowire-coated surfaces with highly wetting liquid, Energy 76 (2014) 428–435.
[49] S. Zhang, Y. Tang, J. Zeng, W. Yuan, J. Chen, C. Chen, Pool boiling heat transfer enhancement by porous interconnected microchannel nets at different liquid subcooling, Appl. Therm. Eng. 93 (2016) 1135–1144.
[50] A.R. Betz, J. Jenkins, C.-J. Kim, D. Attinger, Boiling heat transfer on superhydrophilic, superhydrophobic, and superbiphilic surfaces, Int. J. Heat Mass Transf. 57 (2013) 733–741.
[51] C.M. Kruse, T. Anderson, C. Wilson, C. Zuhlke, D. Alexander, G. Gogos, et al., Enhanced pool-boiling heat transfer and critical heat flux on femtosecond laser processed stainless steel surfaces, Int. J. Heat Mass Transf. 82 (2015) 109–116.
[52] P. Xu, Q. Li, Y. Xuan, Enhanced boiling heat transfer on composite porous surface, Int. J. Heat Mass Transf. 80 (2015) 107–114.
[53] K.Y. Heo, K.D. Kihm, J.S. Lee, Fabrication and experiment of micro-pin-finned microchannels to study surface roughness effects on convective heat transfer, J. Micromech. Microeng. 24 (2014) 125025.
[54] L. Santini, A. Cioncolini, M.T. Butel, M.E. Ricotti, Flow boiling heat transfer in a helically coiled steam generator for nuclear power applications, Int. J. Heat Mass Transf. 92 (2016) 91–99.
[55] G.A. Longo, S. Mancin, G. Righetti, C. Zilio, A new model for refrigerant boiling inside Brazed Plate Heat Exchangers (BPHEs), Int. J. Heat Mass Transf. 91 (2015) 144–149.
[56] G. Son, V.K. Dhir, Numerical simulation of nucleate boiling on a horizontal surface at high heat fluxes, Int. J. Heat Mass Transf. 51 (2008) 2566–2582.